HAL
open science

Chiral plasmonics and enhanced chiral light-matter interactions

Wei Du, Xinglin Wen, Davy Gérard, Cheng-Wei Qiu, Qihua Xiong

To cite this version:

Wei Du, Xinglin Wen, Davy Gérard, Cheng-Wei Qiu, Qihua Xiong. Chiral plasmonics and enhanced chiral light-matter interactions. Science China Physics, Mechanics & Astronomy, 2020, 63 (4), 10.1007/s11433-019-1436-4 . hal-02363361

HAL Id: hal-02363361

https://utt.hal.science/hal-02363361v1

Submitted on 15 Nov 2019

HAL is a multi-disciplinary open access archive for the deposit and dissemination of scientific research documents, whether they are published or not. The documents may come from teaching and research institutions in France or abroad, or from public or private research centers.

L'archive ouverte pluridisciplinaire **HAL**, est destinée au dépôt et à la diffusion de documents scientifiques de niveau recherche, publiés ou non, émanant des établissements d'enseignement et de recherche français ou étrangers, des laboratoires publics ou privés.

Chiral plasmonics and enhanced chiral light-matter interactions

Wei Du[1], Xinglin Wen[1,2], Davy Gérard[3], Cheng-Wei Qiu[4], Qihua Xiong[1,5,6*]*

[1]Division of Physics and Applied Physics, School of Physical and Mathematical Sciences, Nanyang Technological University, Singapore 637371

[2]School of Optical and Electronic Information, Huazhong University of Science and Technology, Wuhan, China 430074

[3]Light, Nanomaterials, Nanotechnologies (L2n), Institut Charles Delaunay, CNRS, Université de Technologie de Troyes, Troyes 10004, France [4]Department of Electrical and Computer Engineering, National University of Singapore, 117583, Singapore

[5]MajuLab, International Joint Research Unit UMI 3654, CNRS, Université Côte d'Azur, Sorbonne Université, National University of Singapore, Nanyang Technological University, Singapore

[6]NOVITAS, Nanoelectronics Center of Excellence, School of Electrical and Electronic Engineering, Nanyang Technological University, Singapore 639798

**Email: qihua@ntu.edu.sg; wenxl@hust.edu.cn*

Abstract:

Chirality, which describes the broken mirror symmetry in geometric structures, exists macroscopically in our daily life as well as microscopically down to molecular levels. Correspondingly, chiral molecules interact differently with circularly polarized light exhibiting opposite handedness (left-handed and right-handed). However, the interaction between chiral molecules and chiral light is very weak. In contrast, *artificial* chiral plasmonic structures can generate "super-chiral" plasmonic near-field, leading to enhanced chiral light-matter (or *chiroptical*) interactions. The "super-chiral" near-field presents different amplitude and phase under opposite handedness incidence, which can be utilized to engineer linear and nonlinear chiroptical interactions. Specifically, in the interaction between quantum emitters and chiral plasmonic structures, the chiral hot spots can favour the emission with a specific handedness. This article reviews the state-of-the-art research on the design, fabrication and chiroptical response of different chiral plasmonic nanostructures or metasurfaces. This review also discusses enhanced chiral light-matter interactions that are essential for applications like chirality sensing, chiral selective light emitting and harvesting. In the final part, the review ends with a perspective on future directions of chiral plasmonics.

Keywords:

Chirality; Chiral plasmonics; Chiral light-matter interactions; Sensing

PACS number(s): 73.20.Mf, 33.55.Ad, 78.20.Ek, 11.30.Rd, 87.80.–y

1. Introduction

Chirality refers to the handedness in geometric structures with a broken mirror symmetry, which exists naturally in varieties of biomolecules, like DNA, enzymes, and proteins, as well as in certain crystals. The two structures or molecules with opposite mirror symmetry are so-called enantiomers, bringing an interesting question yet to be answered, *i.e.*, why often there is only one enantiomer existing in life, such as L-amino acids and D-sugars. Similarly, many drug molecules are also chiral molecules with only one enantiomer suitable for the disease therapy while the other one being functionless or even toxic. Therefore, it is extremely important to develop convenient and efficient techniques for chirality detection. Since the pioneering experiments performed by Pasteur in 1848 [1], it has been understood that the two enantiomers of chiral molecules interact differently with polarized light. As a consequence, optical techniques are widely used to detect chirality, for instance by measuring the rotation of the plane of polarization induced by the chiral medium (as in Pasteur's experiment) or the different absorption of the left circularly polarized light (LCP) or right circularly polarized (RCP) light. The problem lies in the weak chiroptical responses of natural chiral systems, limiting the detection sensitivity. With the advancement of nanofabrication, it is possible to artificially create chiral plasmonic nanostructures or metasurfaces which can generate evanescent fields whose chirality can be much stronger than many natural chiral systems, leading to enhanced chiral light-matter interactions [2-7]. In addition, the chiral plasmonic structure will sustain a "super-chiral" near-field (also termed as chiral "hot spots"). The "super-chiral" near-field will carry different amplitude and phase under RCP and LCP excitations, which can manipulate the circularly polarized light-matter interactions [8]. More importantly, the chirality of the near-field can be imprinted to

the far-field luminescence of the coupled emitters, favouring the emission light into one particular handedness. The progress of chiral plasmonics opens the door for a series of applications, including high-sensitivity chiral detection, chiral selective photoluminescence (PL) manipulation, and chiral selective light harvesting for photocatalysis and photodetection.

Herein we review the state-of-the-art studies on chiral plasmonics and associated chiral light-matter interactions. Section 2 introduces the general design and fabrication of chiral plasmonic geometries, from planar structures to three-dimensional (3D) structures and metasurfaces. The linear and nonlinear chiroptical responses of chiral plasmonic structures will also be discussed in section 2. In section 3, we will focus on the coupling of chiral plasmonic nanostructures to different materials to achieve enhanced chiral light-matter interactions for applications in chirality sensing, circular polarization controlled photoluminescence, and chiral selective hot electron driven light harvesting. Finally, we will end with a short summary together with a future outlook of this field.

2. Chiral plasmonic nanostructures

2.1 Design and fabrication of chiral plasmonic nanostructures

Different types of chiral plasmonic geometries have been designed and fabricated by top-down or bottom-up techniques reported in the literature, such as planar and three dimensional (3D) chiral nanostructures and metasurfaces. For example, Figure 1a shows a planar Au heptamer chiral nanostructure prepared using electron beam lithography technique which exhibits Fano resonance feature in the scattering spectra [9]. At the Fano resonance wavelength, chiroptical effects were observed which can be modulated by adjusting the inter-particle distance and rotation

angle. Figure 1b shows another type of planar metal-insulator-metal (MIM) multilayered chiral nanostructure with Gammadion-shape [10]. The nanostructures with opposite mirror symmetry show reversed circular dichroism effect for the third harmonic generation.

Besides the planar geometries, 3D chiral plasmonic nanostructures have also been widely investigated. For instance, closely spaced metallic nanodisks with different heights have been fabricated using hole-mask colloidal lithography (HCL) [11], as shown in Fig. 1c. In addition to the height differences, the individual nanodisks can also be made of different metals. As a result, the chiroptical properties of such 3D plasmonic oligomers will be determined by the complex interplay between the near-field interactions and phase retardation in these oligomer structures. Figure 1d presents a 3D gold helix structure displaying chiroptical effects on mid-infrared frequencies [12]. Such a structure was achieved by combining direct 3D laser writing technique with electrochemical metal deposition and hence has a limited resolution.

In contrast to lithography techniques which typically require complicated procedures to generate 3D architectures, bottom-up self-assembly methods using chiral molecular template, *e.g.*, DNA or peptide, are more favored in the preparation of 3D chiral plasmonic nanostructures [13,14]. Figure 1e shows an example of left- and right-handed gold nanohelices prepared *via* chiral assembly of gold nanoparticles using a single-stranded DNA as template [15]. The gold nanoparticles are functionalized with different thiol-modified DNA strands that are complementary to the template DNA, allowing the attachment of the gold nanoparticles to the template DNA at a specific attachment site. The chiroptical properties of these assembled gold nanohelices are therefore determined by the collective surface plasmon interactions of accurately positioned nanoparticles in close proximity with chiral arrangement. As

another example of such bottom-up fabrication, Banzer and co-workers [16] have recently demonstrated chirality in trimers made of (achiral) colloidal gold and silicon nanoparticles. In that system, chirality stems from the heterogeneous material composition of the trimer (one gold nanoparticle and two Si nanoparticles). Compared to the planar chiral structure, the 3D chiral structure typically exhibits stronger chiroptical responses. This is because the latter one is a truly 3D chiral structure while the chiral response of the former one mainly comes from the substrate which could induce a small perturbative symmetry-breaking effect. When there is no substrate or when the planar structure is embedded into a uniform matrix, the chirality of the planar structure will disappear. A detailed study has been conducted with planar and 3D starfish chiral structure fabricated with electron beam lithography and on-edge lithography, respectively. Based on the polarization dependent transmission spectra shown in Fig. 1f, the chiral response of the 3D structure is almost two orders of magnitude higher than the planar structure [17].

Last but not least, metasurfaces showing polarization dependent functions under circularly polarized light have also been reported. A metasurface refers to an artificial sheet material with sub-wavelength thickness and spatially varying optical properties determined by the arrangement of the meta-atoms—fundamental building units of the metasurface. By engineering the chiroptical response of the spatially arranged meta-atoms, Fig. 1g shows an example of chiral metasurface based on which reflective chiral meta-holography has been realized [18]. With the same metasurface, different patterns can be reconstructed when illuminating with LCP or RCP. The reflected light keeps the same handedness as the incident circularly polarized light which performs differently from conventional reflectors.

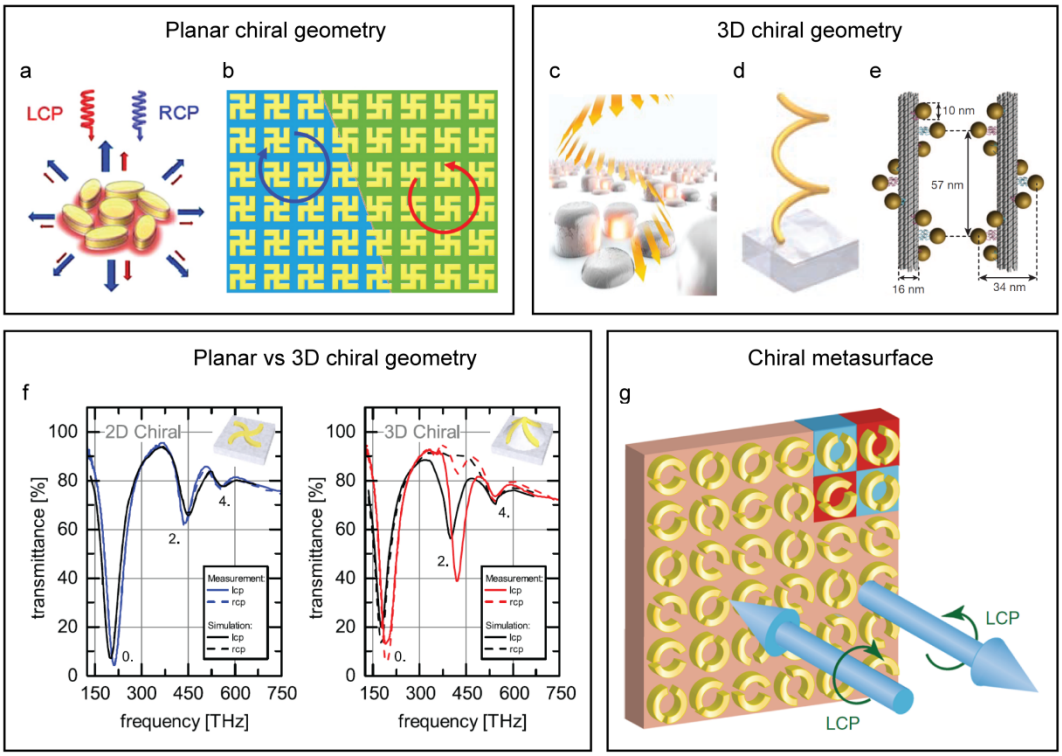

Figure 1. Chiral plasmonic nanostructures. (a) Schematic of a planar Au heptamer chiral nanostructure showing enhanced chiroptical response due to the plasmonic Fano resonance. Reproduced with permission from ref. [9]. (b) Schematic of gammadion-shaped planar MIM nanostructures with mirror symmetry. Reproduced with permission from ref. [10]. (c) Schematic illustration of 3D chiral plasmonic heterotetramers (with different heights for each nanodisk) fabricated with HCL technique. Reproduced with permission from ref. [11]. (d) Schematic of left-handed gold helix nanostructure fabricated with direct 3D laser writing followed by electrochemical deposition. Reproduced with permission from ref. [12]. (e) Schematic of left- and right- handed gold nanoparticle helices fabricated with DNA origami approach. Reproduced with permission from ref. [15]. (f) Comparison of the planar and 3D starfish chiral structure where the latter shows stronger chiroptical effect than the former. Reproduced with permission from ref. [17]. (g) Schematic of a chiral

metasurface for reflective chiral meta-holography. Reproduced with permission from ref. [18].

2.2 Chiroptical effect

Under illumination with circularly polarized light, chiral materials exhibit chiroptical effect due to their different refractive index and extinction coefficient for RCP and LCP. Plasmonic chiral structures with highly twisted evanescent fields also exhibit a chiroptical effect, which could be even stronger than the naturally existent chiral systems. Three frequently discussed chiroptical effects are circular birefringence (CB), circular dichroism (CD) and asymmetric transmission.

CB refers to the optical rotation of polarization of the linearly polarized light transmitted through a chiral medium where the rotation direction (clockwise or counterclockwise) is determined by the handedness of the chiral material. The linear polarization rotation stems from the different phase velocities for RCP and LCP light when interacting with one certain chiral structure. As linearly polarized light can be treated as a combination of RCP and LCP light, the RCP and LCP components keep the same amplitude but have different phase velocities when transmitting in the chiral medium, resulting in the linear polarization rotation. Figure 2a shows the experimental scheme of the CB measurement and Figure 2b provides the measured rotation angles for the achiral plasmonic structure and chiral plasmonic structure of different handedness [19]. Opposite rotation direction was observed with the left- and right- handed chiral structure while no rotation was observed with the achiral structure.

CD refers to the differential absorption or transmission of RCP or LCP which is frequently used for chirality sensing. Figure 2c shows the schematic of the achiral and chiral optical antennas and Fig. 2d presents the experimentally measured chirality

flux and CD spectra of the achiral and chiral antennas in the far field [20]. The chirality flux is linked to chiral near-field and can be determined by detecting the CD of the scattered light in the far field. Although both spectra show a clear difference between achiral and chiral antennas with opposite handedness, their magnitude and resonant wavelengths differ from each other as they actually contain different information. CD spectrum is measured with circularly polarized incident light which reflects the alteration of the chiral light by the sample and mainly provides chirality information of the sample. In contrast, linearly polarized incident light is used for the chirality flux spectrum which could measure the capability of the sample to create chiral fields.

Asymmetric transmission points to the different RCP to LCP or LCP to RCP conversion efficiencies. Figure 2e shows the schematic diagram of a planar plasmonic metasurface composed of L-shaped gold nanostructures arranged in a square lattice [21]. The designed metasurface could transmit and simultaneously reverse the spin of incident RCP, but reflect and meanwhile maintain the spin of incident LCP. In other words, RCP can be converted into LCP with the above metasurface while LCP will be reflected as LCP. Such an asymmetric transmission is proved experimentally and can be clearly visualized in the measured circular polarization resolved transmission spectra shown in Fig. 2f.

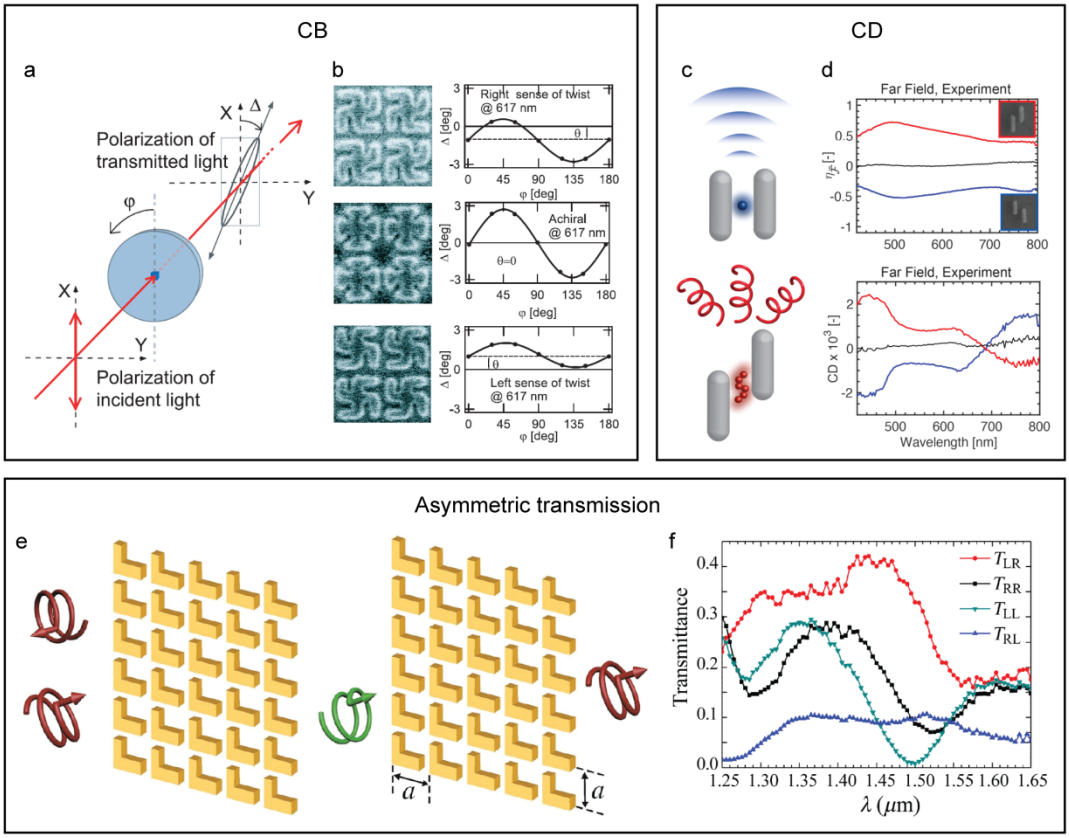

Figure 2. Linear chiroptical effects. (a) Schematic illustration of the CB measurement. (b) Optical rotation angles measured from plasmonic planar nanostructures with left-handedness, achiral geometry, and right-handedness. a and b are reproduced with permission from ref. [19]. (c) Schematic illustration of achiral and chiral optical antennas. (d) Comparison of chirality flux spectra and CD spectra measured from the achiral and chiral optical antennas. c and d are reproduced with permission from ref. [20]. (e) Schematic of a planar plasmonic metasurface with a designed asymmetric transmission. (f) Circular polarization resolved transmission spectra measured with the metasurface in (e). (e) and (f) are reproduced with permission from ref. [21].

Besides the above linear chiroptical effects, nonlinear chiroptical effects such as the different second harmonic generation (SHG) or third harmonic generation

(THG) signals under RCP and LCP incident light have also been reported in chiral plasmonic systems [22-26]. The nonlinear interaction between near-field and chiral light is usually three orders of magnitude stronger than linear interaction. For example, CD in the SHG signal has been well reported for chiral plasmonic nanostructures with a "G" shape [22]. Figure 3a and 3d show the SEM images of two types of G-shaped Au nanostructures arranged in opposite mirror symmetry. From the SHG microscopy images shown in Fig. 3b-c and Fig. 3e-f recorded from the two structures respectively, some "hot spots" were observed whose intensity and distribution depend on the circular polarization of the incident light, leading to the CD effect of the SHG. As a result, the CD of SHG is intrinsically sensitive to the geometric arrangement of these "G-shaped" structures which directly determines the position and intensity of SHG hot spots under particular circularly polarized light. The origin of the SHG enhancement in this case can be attributed to a strong local enhancement of the EM field at the fundamental frequency. On the contrary, the SHG mapping can provide the distribution of the chiral hot spots.

Similarly, CD in the THG signal was also demonstrated with a Gammadion-shaped chiral plasmonic structure of C4 rotational symmetry which was chosen based on the selection rule for THG [23]. Figure 3g shows the working principle of the Gammadion-shaped chiral structure with C4 rotational symmetry. Under LCP incident light, no THG will be generated. Under RCP incident light, THG with opposite polarization will be generated. Figure 3h shows the polarization-dependent THG spectra recorded under incident LCP and RCP while the calculated CD of THG is shown in Fig. 3i. The experimental results agree with the working principle illustrated in Fig. 3g. Usually in 2D planar metasurface, an oblique excitation was utilized to induce the nonlinear susceptibility along z-direction which arises from the

substrate induced asymmetry. However, in this experiment, the excitation laser was normal to the substrate to eliminate the z-direction nonlinear components. A near unity nonlinear CD can be achieved only by the in-plane nonlinear tensor components. The nonlinear chiral interaction is much stronger than the linear chiral interaction in planar chiral structure.

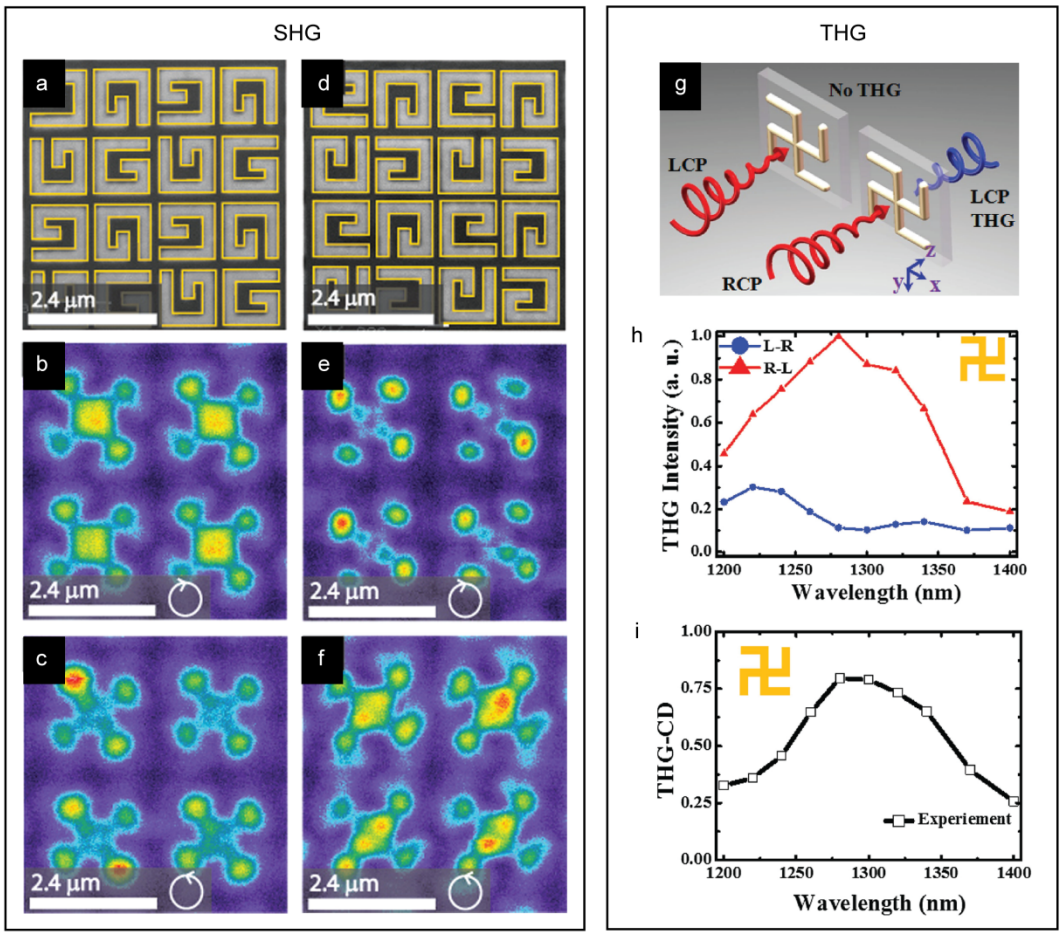

Figure 3. Nonlinear chiroptical effects. (a, b, c) SEM image and SHG microscopy images for the "G-shaped" plasmonic structure. (d, e, f) SEM image and SHG microscopy images for the "mirror-G-shaped" plasmonic structure. a-f are reproduced with permission from ref. [22]. (g) Schematic illustration of the THG generation in a Gammadion-shaped plasmonic structure with C4 rotational symmetry. (h-i) Polarization-dependent THG spectra with circularly polarized incident light and

corresponding calculated CD of THG. g-i are reproduced with permission from ref. [23].

3. Chiral selective light-matter interactions based on chiral plasmonic nanostructures

3.1 Chiral plasmonics enhanced chiral molecule sensing

As mentioned before, the fundamental units of life are chiral biomolecules. A lot of drugs also contain molecular units with specific chirality. Enantiomers often exhibit handedness dependent functions, making it strikingly important to detect the chirality of molecules. However, due to the weak chiroptical response of the natural chiral molecules, chiral molecule sensing is often challenging at low molecular concentration. Artificial chiral plasmonic nanostructures or metasurfaces own the capability to generate superchiral electromagnetic fields, leading to promising application for ultrasensitive chiral biomolecule sensing [27-31]. For example, a planar plasmonic chiral metamaterial (PCM) has been used as probes for the detection of large chiral biomolecules with high sensitivity, with the SEM image and CD response of the bare PCM shown in Figure 4a [30]. Three resonances were observed in the CD spectra, corresponding to the different localized surface plasmon resonances (LSPRs) supported by the PCM. After adsorption of biomolecules, the change in the refractive index could induce shifts in the LSPRs which would in turn modulate the CD spectra of the PCM. Figure 4b shows the CD spectra of the PCMs before (red curve) and after (black curve) adsorption of β-lactoglobulin as an example. Based on the biomolecule induced shift in the CD spectra with PCM of opposite handedness, asymmetry in the refractive index of the biomolecule could be extracted which tells the chirality of the biomolecule. With such a PCM, the detection

sensitivity could be largely enhanced, allowing chiral molecule sensing at the picogram level.

Benefiting from the high sensitivity, superchiral evanescent fields of plasmonic chiral structures have also been utilized to probe ligand induced conformational changes in the higher order hierarchical structure of proteins [31]. Figure 4c shows one type of protein, 5-enolpyruvylshikimate 3-phosphate synthase (EPSPS) in open format (left) without the presence of ligand, which will transfer to the closed format (right) after ligand binding. Figure 4d shows the geometry of the chiral plasmonic nanostructure used for the protein higher order structure detection, which supports superchiral field that is one order of magnitude higher than circularly polarized light. The changes in the optical rotations of the chiral plasmonic structure induced by EPSPS adsorption and further ligand binding are clearly seen in Figure 4e. Such a level of detection could not be achieved with conventional optical polarimetry technique without relying on chiral plasmonic field.

Another approach for chiral molecule sensing is to make use of the chiral molecule triggered self-assembly of plasmonic nanostructures [32-35]. In that case, the fundamental building block can be achiral plasmonic nanostructure, like nanoparticle or nanorod, which after self-assembly under the existence of the chiral analyte could generate chiral plasmonic field. Using standard chirality detection technique, such as CD spectroscopy, the self-assembly induced chiroptical response could be followed which reveals the property of the chiral analyte. Figure 4f shows the schematic of a chiral nanoparticle heterodimer composed of an Au nanoparticle and an Ag nanoparticle bridged by chiral molecule [32]. The chirality of the nanoparticle heterodimer originates from the distinct dihedral angle between the two individual nanoparticles, as shown in Fig. 4g. The dihedral angle with an opposite

sign leads to chiral plasmonic nanostructure of opposite symmetry, *i.e.*, left-handedness or right-handedness, which is directly determined by the chirality of the bridge molecule. Based on this principle, Figure 4h shows the measured CD signal induced by the chiral self-assembly of the nanoparticle heterodimer triggered by a protein, prostate-specific antigen (PSA), which is a widely used cancer biomarker. The CD signal increases with increasing concentration of PSA analyte, due to the increased self-assembly yield of nanoparticle heterodimers.

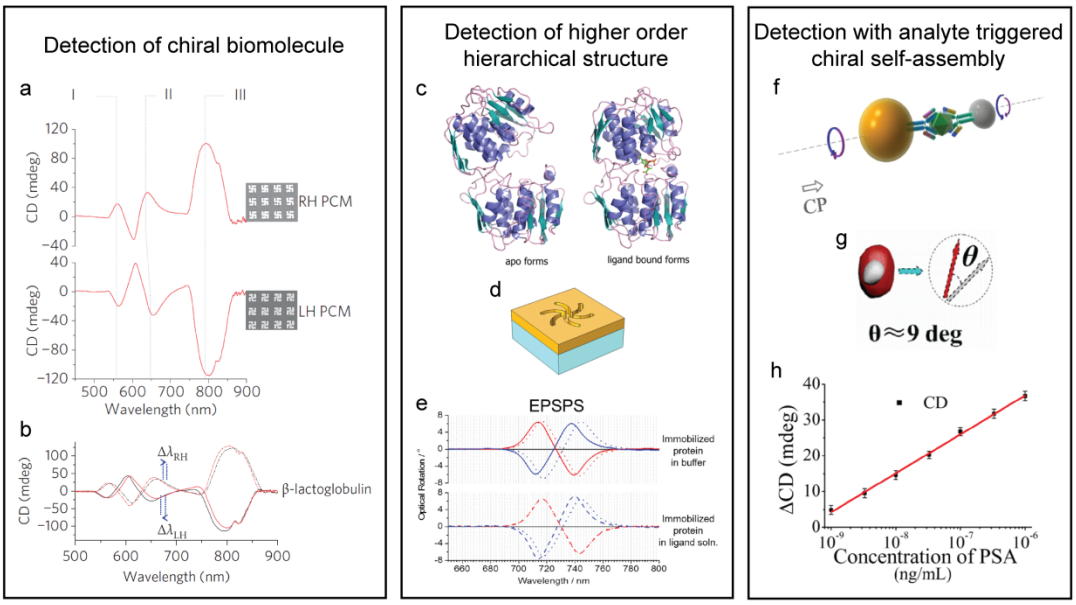

Figure 4. Enhanced chiral molecule sensing based on super-chiral fields. (a) SEM images and CD spectra for right- and left-handed PCMs. (b) Modulation of CD spectra induced by adsorption of β–lactoglobulin. a and b are reproduced with permission from ref. [30]. (c) EPSPS crystal structures in open (left) and closed (right) format without and with ligands. (d) Schematic illustration of the chiral plasmonic nanostructure used for the sensing of EPSPS higher order structure. (e) Changes in measured optical rotation due to immobilized protein and further conformation changes of protein induced by ligand. c, d and e are reproduced with permission from ref. [31]. (f) Schematic illustration of the chiral nanoparticle heterodimer self-

assembled via chiral molecular bridge. (g) Schematic illustration of the distinct dihedral angle between the two individual nanoparticles determining the chirality of the nanoparticle heterodimer. (h) Measured CD response of the nanoparticle heterodimers self-assembled in the presence of PSA of different concentration. f, g and h are reproduced with permission from ref. [32].

3.2 Chiral plasmonics modulated quantum emission

By integrating chiral plasmonic nanostructures with quantum emitters, the chiral light-matter interaction enables chiral selective or artificial chiral quantum emission which will find applications in quantum communication, bio-sensing and bio-imaging. In principle, the super-chiral field can be quantitatively described by the optical chirality density C, $C = -\frac{\varepsilon_0 \omega}{2}(E^* \bullet B)$, where E and B denote the complex electric and magnetic field vectors, respectively [8]. The optical chirality density can be seen as an equivalent of the local density of states (LDOS) in electromagnetics, which modifies the emission rate of the quantum emitters via Purcell effect [36]. It should be noted that there is another explanation that the emitters can simply couple to the chiral eigenmodes of the plasmonic nanoantenna, and then emit polarized photons [37]. In detail, the chiral plasmonic nanostructures could influence the chiral response of the quantum emitters in two ways. On one hand, it could induce increased absorption of one particular circularly polarized light depending on the chirality of the plasmonic field, resulting in chiral selective enhancement of PL emission. On the other hand, the chirality of the plasmonic nanostructures also results in a preferred spin state in the PL emission, leading to direct circularly polarized light emission. Controlling resonant interaction condition is important to ensure a strong chiral light-matter interaction in the hybrid system, which requires a frequency overlap between

the resonance of the chiral plasmonic nanostructure and the absorption (or emission) of the quantum emitter.

Figure 5a-b shows the polarization-resolved PL spectra from achiral semiconductor quantum dots with and without the existence of the chiral plasmonic metasurface [38]. Circularly polarized PL emission (with the degree of circular polarization of 17%) was achieved in the presence of the chiral metasurface while PL of a negligible degree of circular polarization was obtained in the absence of the chiral metasurface. Not only normal PL, but also two-photon luminescence (TPL), which belongs to a nonlinear signal, could be efficiently modified by the chiral plasmonic near field. The chiral selective enhancement of TPL in CdTe/ZnS core-shell QDs have been demonstrated with a chiral arc-shaped plasmonic metasurface, with SEM images of the two enantiomers shown in the inset of Fig. 5c and Fig. 5d [39]. With a specific plasmonic enantiomer, the TPL enhancement shows a clear contrast for the excitation with LCP or RCP, as shown in Fig. 5c for right-handed enantiomer and Fig. 5d for left-handed enantiomer. The chiral emission from the achiral semiconductor holds great potential in applications of spintronics, quantum communication, light sources, and so on.

Furthermore, the superchiral evanescent field of chiral plasmonic nanostructures has also been used for tailoring the valley-polarized PL emission in two-dimensional transition metal dichalcogenides (TMDs) [40-42]. This type of materials owns intrinsic spin–valley degree of freedom and can be useful for developing spintronic and valleytronic devices [43-45]. Generally, the TMD monolayer has two degenerate but inequivalent valleys (K and K') which prefer to couple to RCP or LCP, respectively. Under incident circularly polarized light excitation, valley-polarized PL emission has been reported for TMDs [46-48]. The

degree of valley polarization (DVP), is commonly used to describe the purity of the valley-polarized PL emission, which is defined as DVP = $(I_{\sigma+}-I_{\sigma-})/(I_{\sigma+}+I_{\sigma-})$. $I_{\sigma+}$ and $I_{\sigma-}$ correspond to the circular polarization resolved PL intensities. The intrinsic DVP of TMD monolayer is usually not high due to the phonon-assisted intervalley scattering. However, in a recent study, with the designed chiral plasmonic metasurface, DVP of chemical vapour deposited MoS_2 monolayer was increased from 25% ± 2% to 43% ± 2% under LCP excitation and decreased to 20% ± 2% under RCP excitation [41]. The mechanism of the chiral plasmonic modulation of DVP is explained in Fig. 5e and Fig. 5f, which shows the energy band of the MoS_2 monolayer without and with the presence of the chiral plasmonic metasurface, respectively. For the bare MoS_2 monolayer, under the incident LCP (or RCP) light, exciton formation in the K′ (or K) valley is preferred. A small part of the excitons in the K′ (or K) valley can jump to the opposite K (or K′) valley via phonon assisted intervalley scattering. In the end, more exciton emission happens in the K′ (or K) valley than in the opposite one, resulting in intrinsic valley-polarized PL emission of MoS_2 monolayer. However, in the presence of chiral plasmonic metasurface with left-handedness, there will be two different results. When the hybrid system is excited with LCP, the exciton formation in K′ valley will be enhanced. The phonon assisted intervalley scattering from K′ to K valley may also increase a bit, but not as much as the increased exciton formation rate in K′ valley. Simultaneously, the exciton emission in K′ valley is also enhanced while the opposite happens in K valley. Therefore, the overall effect will be increased DVP under LCP excitation. On the contrary, when RCP excitation is adopted, the mismatch between the chirality of the plasmonic field and the chirality of the incident light will lead to decreased DVP. Figure 5g shows the experimental results of DVP for bare MoS_2 and MoS_2-metasurface hybrid system under LCP and

RCP excitation, which agree with the expected one. Moreover, as shown in Fig. 5h, when using linearly polarized incident light, circularly polarized PL emission was only observed from the hybrid system, but not for bare MoS_2, which directly reveals the superchiral near field generated by the chiral plasmonic metasurface.

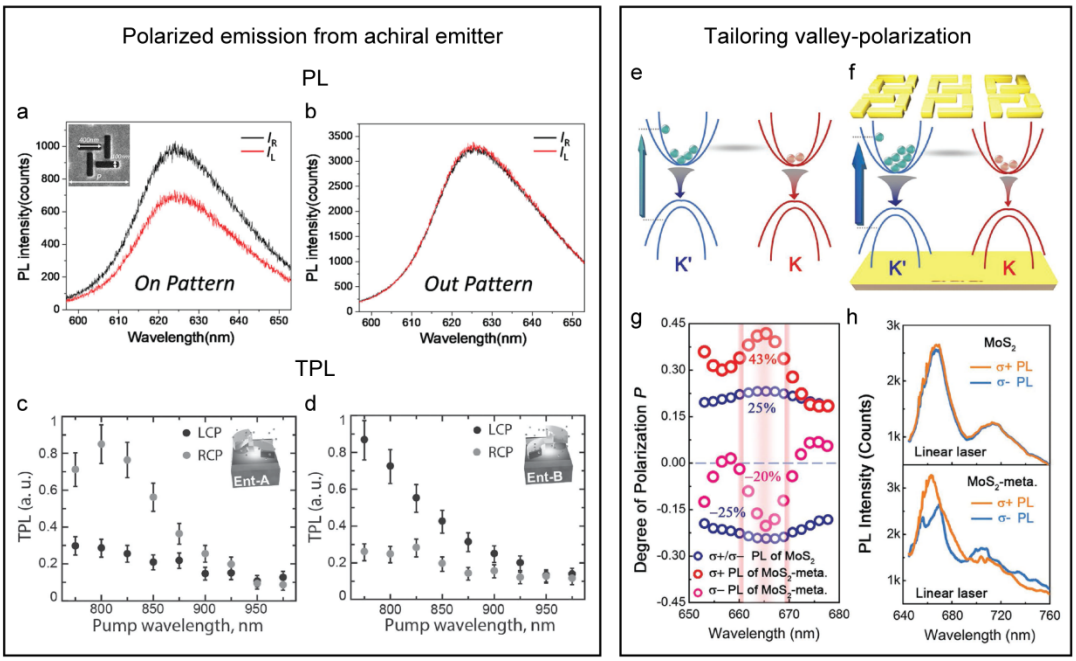

Figure 5. Chiral plasmonics modulated quantum emission. (a, b) Measured circular polarization resolved PL spectra for achiral semiconductor quantum dots with (a) and without (b) the chiral plasmonic metasurface. Inset shows the SEM image of the building block for the chiral plasmonic metasurface. a and b are reproduced with permission from ref. [38]. (c) TPL enhancement with right-handed chiral plasmonic metasurface under LCP and RCP excitation. Inset shows the SEM image of the right-handed chiral plasmonic metasurface. (d) TPL enhancement with left-handed chiral plasmonic metasurface under LCP and RCP excitation. Inset shows the SEM image of the left-handed chiral plasmonic metasurface. c and d are reproduced with permission from ref. [39]. (e, f) Schematic illustration of the energy band for bare MoS_2 monolayer (e) and MoS_2-chiral plasmonic metasurface hybrid system (f). (g)

Experimentally measured DVP for bare MoS_2 monolayer and MoS_2-chiral plasmonic metasurface hybrid system under LCP and RCP excitation. (h) Circular polarization resolved PL spectra with linearly polarized laser excitation. e-h are reproduced with permission from ref. [41].

3.3 Chiral selective hot electron transfer

Plasmonic hot electrons are generated during the non-radiative decay of surface plasmons. They have higher kinetic energy and are excited in larger numbers than the normally optically excited electrons, so that they can overcome the potential barrier to be injected into semiconductors to drive a wide range of applications, such as photodetection, solar energy harvesting, and photocatalysis [49,50]. In addition, the timescale of the plasmonic hot electron generation is around hundreds of femtoseconds, which ensures the great potential of plasmonic hot electrons for applications in ultrafast optical switches and modulators. With engineered artificial chiral plasmonic nanostructures or metasurfaces, chiral selective hot electron transfer offers the opportunity for convenient detection of circularly polarized light and enantioselective catalysis [51-53].

For example, Fig. 6a shows the schematic of a circularly polarized light detector based on chiral selective hot electron transfer in designed chiral plasmonic metamaterial in contact with a semiconductor [51]. The chiral plasmonic metamaterial has a MIM structure with PMMA layer sandwiched between a “Z-shaped” Ag antenna and a flat Ag film. The Ag antenna is in contact with n-type Si to form the Schottky junction, allowing plasmonic hot electron injection. When the chirality of the plasmonic metamaterial matches with the chirality of the incident circularly polarized light, the efficiency of the hot electron generation and transfer is higher than

the other case with opposite chirality. Figure 6b-c shows the experimental and theoretical responsivity of the circularly polarized light detector for chiral plasmonic metamaterial with opposite symmetry. The left-handed metamaterial shows clearly enhanced photoresponsivity under LCP illumination than RCP while the opposite phenomenon was observed with right-handed metamaterial.

Figure 6d shows another work studying chiral selective hot electron transfer utilizing chiral split-ring plasmonic nanoresonator integrated with TiO_2 semiconductor [52]. The dichroism of the incident photon-to-charge conversion efficiency (IPCE) under circularly polarized incident light, as shown in Fig. 6e, shows a similar shape to the CD response of the sample measured based on extinction. Further, Fig. 6f presents the dichroism of the cathodoluminescence (CL) spectrum measured from the chiral split-ring plasmonic nanoresonator. Based on the dichroic-sensitive CL imaging, the chiral response of the split-ring structure was attributed to the polarization dependent distributions of electric field hot spots. It was also found that there is a clear positive correlation between the calculated plasmonic hot carrier distribution and the spatial distributions of CL signal, pointing to the application of CL imaging technique for the rational design of hot electron based devices.

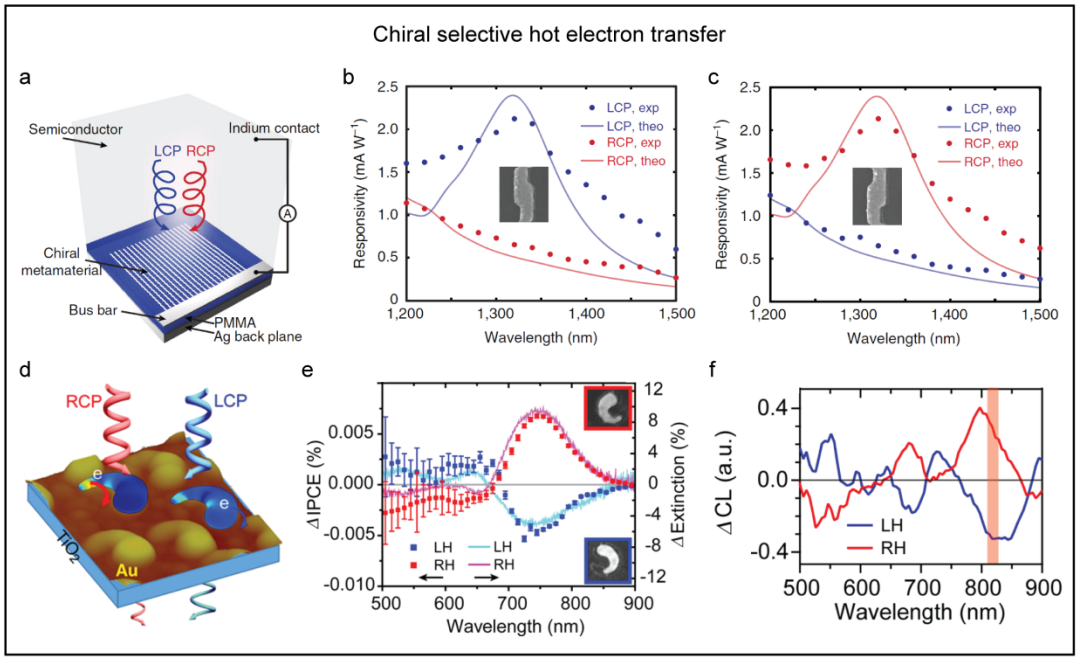

Figure 6. Chiral selective hot electron transfer. (a) Schematic illustration of the circularly polarized light detector composted of a plasmonic chiral metamaterial in contact with n-type Si semiconductor. (b,c) Experimental and theoretical responsivity of the photodetector with left- (b) and right- (c) handed metamaterial under the illumination of circularly polarized light. a-c are reproduced with permission from ref. [51]. (d) Schematic illustration of chiral selective hot electron transfer at the interface between chiral split-ring plasmonic nanoresonator and TiO_2. (e) CD of IPCE and CD of extinction measured from the same device. (f) CD of CL for the chiral split-ring plasmonic nanoresonator. d-f are reproduced with permission from ref. [52].

Though various chiral structures are realized in different studies, they share the same principle that the chirality is originated from the mirror symmetry break of the structure and can be quantified with the optical chirality density as we discussed. In order to optimize the chiral light-matter interaction, the resonance wavelength of the chiral structure must be matched with the emission or absorption wavelength of the emitter, or matched with the excitation laser wavelength.

4. Conclusion

In summary, this article provides a brief review on the current progress of chiral plasmonics and associated chiral light-matter interactions for applications in biosensing, PL modulation and hot-electron based light harvesting. Here we hope to propose some future research directions for this field.

Regarding chiral sensing, the enhanced sensitivity is the most remarkable feature for biomolecule sensing with chiral plasmonic nanostructures or metasurfaces. However, the reported sensitivity, as we know, requires at least several tens of molecules per unit structure [29]. Hence, single molecule detection with single chiral plasmonic nanoantenna would be one of the future directions in this field. Such detection may be facilitated by chiral molecules containing emitting group. Since single molecule photoluminescence has been widely investigated [54], the chiroptical response in PL will tell the chirality of the studied molecule.

Chiral selective chemical or biological reaction will be extremely important and definitely worth continuous efforts. It is well-known that a lot of biomolecules and drugs are chiral molecules that the two enantiomers often exhibit very different functions. Currently, the fabrication or synthesis products are typically mixture of the two enantiomers such that complex separation procedures are needed to select the one with preferred function. It would be great if the coupling with chiral plasmonic nanostructures could guide the chiral selective synthesis of only one of the two enantiomers.

The angular momentum of light contains two freedom, namely, the spin and orbital angular momentum (SAM and OAM). The SAM is related to the circular polarization while the OAM is associated with the helical phase of the light. SAM and

OAM of the light can be encoded for the light communication. The chiral plasmonic structures offer the possibility to engineer the SAM and OAM and the interaction between them. It has been reported that the spin of light can control the OAM by utilizing the nonlinearity of the chiral metasurface [25]. The chiral plasmonic controlled angular momentum of light holds great research interest in the future.

Another promising direction is chiral plasmonic circuit which enables circular polarization controlled on-chip information communication and processing. The principle of unidirectional surface plasmon propagating or routing controlled by circularly polarized light has been demonstrated in the literature [55, 56]. On one hand, direct circularly polarized light emission from chiral plasmonics coupled quantum emitters was reported [38, 41, 42] which can be used as the plasmon source in the integrated chiral plasmonic chip. On the other hand, chiral plasmon detector can be made of chiral plasmonic nanostructures in contact with semiconductor which works based on the chiral selective hot electron transfer [51, 52]. By combing these different elements together, the simplest optically or electrically driven chiral plasmonic circuit is ready to be developed.

The development of artificial chiral nanostructures will also require new approaches to probe chirality at the nanoscale. Up to this work, reported works used near-field optical microscopy [57] and cathodoluminescence [58] to image chiral optical fields with sub-wavelength resolution. Electron spectroscopies, and notably electron energy-loss spectroscopy (EELS) has recently emerged as a powerful tool for the nanoscale analysis of plasmonic structures [59]. It was theoretically demonstrated that phase-shaped (vortex) electron beams could probe dichroism via a transfer of OAM between the electron beam and the chiral structure [60]. As very recent experimental developments using magnetic phase plates have demonstrated the

generation of electron vortex beams [61], the possibility to probe and map the chiral modes of plasmonic nanostructures inside an electron microscope now seems feasible.

Last but not the least, time-scale studies, such as time-resolved PL or pump-probe spectroscopy, may be used to trace the dynamics of self-assembly with chiral template, chiral selective PL enhancement or hot electron transfer, providing useful information for better understanding of the chiral light-matter interactions.

This work was supported by Singapore National Research Foundation - Agence Nationale de la Recherche (NRF2017-NRF-ANR005 2D-CHIRAL).

References

1. L. Pasteur, *Ann. Chim. Phys.* **24**, 442 (1848).
2. S. Yoo, and Q. Park, *Nanophotonics* **8,** 249 (2019).
3. M. Hentschel, M. Schäferling, X. Duan, H. Giessen, and N. Liu, *Sci. Adv.* **3,** e1602735 (2017).
4. Y. Luo, C. Chi, M. Jiang, R. Li, S. Zu, Y. Li, and Z. Fang, *Adv. Opt. Mater.* **5,** 1700040 (2017).
5. V. K. Valev, J. J. Baumberg, C. Sibilia, and T. Verbiest, *Adv. Mater.* **25,** 2517 (2013).
6. Z. Wang, F. Cheng, T. Winsor, and Y. Liu, *Nanotechnology* **27,** 412001 (2016).
7. X. Wang, and Z. Tang, *Small* **13,** 1601115 (2017).
8. M. Schäferling, D. Dregely, M. Hentschel, and H. Giessen, *Phys. Rev. X* **2,** 031010 (2012).
9. S. Zu, Y. Bao, and Z. Fang, *Nanoscale* **8,** 3900 (2016).
10. C. Zhang, Z. Li, X. Yang, Z. Chen, and Z. Wang, *AIP Adv.* **6,** 125014 (2016).

11. R. Ogier, Y. Fang, M. Svedendahl, P. Johansson, and M. Käll, *ACS Photonics* **1,** 1074 (2014).

12. J. K. Gansel, M. Thiel, M. S. Rill, M. Decker, K. Bade, V. Saile, G. von Freymann, S. Linden, and M. Wegener, *Science* **325,** 1513 (2009).

13. X. Lan, and Q. Wang, *Adv. Mater.* **28,** 10499 (2016).

14. H. E. Lee, H. Y. Ahn, J. Lee, and K. T. Nam, *ChemNanoMat.* **3,** 685 (2017).

15. A. Kuzyk, R. Schreiber, Z. Fan, G. Pardatscher, E. M. Roller, A. Högele, F. C. Simmel, A. O. Govorov, and T. Liedl, *Nature* **483,** 311 (2012).

16. P. Banzer, P. Wozniak, U. Mick, I. De Leon, and R. W. Boyd, *Nat. Commun.* **7**, 13117 (2016).

17. K. Dietrich, C. Menzel, D. Lehr, O. Puffky, U. Hübner, T. Pertsch, A. Tünnermann, and E. B. Kley, *Appl. Phys. Lett.* **104,** 193107 (2014).

18. Q. Wang, E. Plum, Q. Yang, X. Zhang, Q. Xu, Y. Xu, J. Han, and W. Zhang, *Light Sci. Appl.* **7,** 25 (2018).

19. M. Kuwata-Gonokami, N. Saito, Y. Ino, M. Kauranen, K. Jefimovs, T. Vallius, J. Turunen, and Y. Svirko, *Phys. Rev. Lett.* **95,** 227401 (2005).

20. L. V. Poulikakos, P. Thureja, A. Stollmann, E. De Leo, and D. J. Norris, *Nano Lett.* **18,** 4633 (2018).

21. W. Ye, X. Yuan, C. Guo, J. Zhang, B. Yang, and S. Zhang, *Phys. Rev. Appl.* **7,** 054003 (2017).

22. V. K. Valev, N. Smisdom, A. V. Silhanek, B. De Clercq, W. Gillijns, M. Ameloot, V. V. Moshchalkov, and T. Verbiest, *Nano Lett.* **9,** 3945 (2009).

23. S. Chen, F. Zeuner, M. Weismann, B. Reineke, G. Li, V. K. Valev, K. W. Cheah, N. C. Panoiu, T. Zentgraf, S. Zhang, *Adv. Mater.* **28,** 2992 (2016).

24. S. P. Rodrigues, S. Lan, L. Kang, Y. Cui, and W. Cai, *Adv. Mater.* **26,** 6157

(2014).

25. G. Li, L. Wu, K. F. Li, S. Chen, C. Schlickriede, Z. Xu, S. Huang, W. Li, Y. Liu, E. Y. B. Pun, T. Zentgraf, K. W. Cheah, Y. Luo, and S. Zhang, *Nano Lett.* **17,** 7974 (2017).

26. V. K. Valev, J. J. Baumberg, B. De Clercq, N. Braz, X. Zheng, E. J. Osley, S. Vandendriessche, M. Hojeij, C. Blejean, J. Mertens, C. G. Biris, V. Volskiy, M. Ameloot, Y. Ekinci, G. A. E. Vandenbosch, P. A. Warburton, V. V. Moshchalkov, N. C. Panoiu, and T. Verbiest, *Adv. Mater.* **26,** 4074 (2014).

27. J. Kumar, and L. M. Liz-marzán, *Bull. Chem. Soc. Jpn.* **92,** 30 (2019).

28. V. E. Bochenkov, and T. I. Shabatina, *Biosensors* **8,** 120 (2018).

29. Y. Zhao, A. N. Askarpour, L. Sun, J. Shi, X. Li, and A. Alù, *Nat. Commun.* **8,** 14180 (2017).

30. E. Hendry, T. Carpy, J. Johnston, M. Popland, R. V. Mikhaylovskiy, A. J. Lapthorn, S. M. Kelly, L. D. Barron, N. Gadegaard, and M. Kadodwala, *Nat. Nanotechnol.* **5,** 783 (2010).

31. R. Tullius, A. S. Karimullah, M. Rodier, B. Fitzpatrick, N. Gadegaard, L. D. Barron, V. M. Rotello, G. Cooke, A. Lapthorn, and M. Kadodwala, *J. Am. Chem. Soc.* **137,** 8380 (2015).

32. X. Wu, L. Xu, L. Liu, W. Ma, H. Yin, H. Kuang, L. Wang, C. Xu, and N. A. Kotov, *J. Am. Chem. Soc.* **135,** 18629 (2013).

33. W. Ma, H. Kuang, L. Xu, L. Ding, C. Xu, L. Wang, and N. A. Kotov, *Nat. Commun.* **4,** 2689 (2013).

34. Z. Xu, L. Xu, Y. Zhu, W. Ma, H. Kuang, L. Wang, and C. Xu, *Chem. Commun.* **48,** 5760 (2012).

35. B. Han, Z. Zhu, Z. Li, W. Zhang, and Z. Tang, *J. Am. Chem. Soc.* **136,** 16104

(2014).

36. G. Colas des Francs, J. Barthes, A. Bouhelier, J. C. Weeber, A. Dereux, A. Cuche, and C. Girard, *J. Opt.* **18**, 094005 (2016).

37. N. Meinzer, E. Hendry, and W. L. Barnes, *Phys. Rev. B* **88***,* 041407 (2013).

38. Z. Wang, Y. Wang, G. Adamo, J. Teng, and H. Sun, *Laser Photon. Rev.* **13**, 1800276 (2019).

39. S. P. Rodrigues, Y. Cui, S. Lan, L. Kang, and W. Cai, *Adv. Mater.* **27,** 1124 (2015).

40. Z. Li, Y. Li, T. Han, X. Wang, Y. Yu, B. Tay, Z. Liu, and Z. Fang, *ACS Nano* **11,** 1165 (2017).

41. Z. Li, C. Liu, X. Rong, Y. Luo, H. Cheng, L. Zheng, F. Lin, B. Shen, Y. Gong, S. Zhang, and Z. Fang, *Adv. Mater.* **30,** 1801908 (2018).

42. H. T. Lin, C. Y. Chang, P. J. Cheng, M. Y. Li, C. C. Cheng, S. W. Chang, L. L. J. Li, C. W. Chu, P. K. Wei, and M. H. Shih, *ACS Appl. Mater. Interfaces* **10,** 15996 (2018).

43. X. Xu, W. Yao, D. Xiao, and T. F. Heinz, *Nat. Phys.* **10,** 343 (2014).

44. J. R. Schaibley, H. Yu, G. Clark, P. Rivera, J. S. Ross, K. L. Seyler, W. Yao, and X. Xu, *Nat. Rev. Mater.* **1,** 16055 (2016).

45. K. F. Mak, D. Xiao, and J. Shan, *Nat. Photonics* **12,** 451 (2018).

46. A. Singh, K. Tran, M. Kolarczik, J. Seifert, Y. Wang, K. Hao, D. Pleskot, N. M. Gabor, S. Helmrich, N. Owschimikow, U. Woggon, and X. Li, *Phys. Rev. Lett.* **117,** 257402 (2016).

47. W. T. Hsu, Y. L. Chen, C. H. Chen, P. S. Liu, T. H. Hou, L. J. Li, and W. H. Chang, *Nat. Commun.* **6,** 8963 (2015).

48. A. Neumann, J. Lindlau, L. Colombier, M. Nutz, S. Najmaei, J. Lou, A. D.

Mohite, H. Yamaguchi, and A. Högele, *Nat. Nanotechnol.* **12,** 329 (2017).

49. M. L. Brongersma, N. J. Halas, and P. Nordlander, *Nat. Nanotechnol.* **10,** 25 (2015).

50. C. Clavero, *Nat. Photonics* **8,** 95 (2014).

51. W. Li, Z. J. Coppens, L. V. Besteiro, W. Wang, A. O. Govorov, and J. Valentine, *Nat. Commun.* **6,** 8379 (2015).

52. Y. Fang, R. Verre, L. Shao, P. Nordlander, and M. Käll, *Nano Lett.* **16,** 5183 (2016).

53. C. Hao, L. Xu, W. Ma, X. Wu, L. Wang, H. Kuang, and C. Xu, *Adv. Funct. Mater.* **25,** 5816 (2015).

54. S. Weiss, *Science* **283,** 1676 (1999).

55. J. Lin, J. P. B. Mueller, Q. Wang, G. Yuan, N. Antoniou, X. C. Yuan, and F. Capasso, *Science* **340,** 331 (2013).

56. S. H. Gong, F. Alpeggiani, B. Sciacca, E. C. Garnett, and L. Kuipers, *Science* **359,** 443 (2018).

57. T. Narushima, and H. Okamoto, *J. Phys. Chem. C* **117**, 23964 (2013).

58. S. Zu, T. Han, M. Jiang, F. Lin, X. Zhu, Z. Fang, *ACS Nano* **12**, 3908 (2018).

59. M. Kociak, and O. Stéphan, *Chem. Soc. Rev.* **43**, 3865 (2014).

60. A. Asenjo-Garcia, and F. J. G. de Abajo, *Phys. Rev. Lett.* **113**, 066102 (2014).

61. G. Guzzinati, A. Béché, H. Lourenço-Martins, J. Martin, M. Kociak, and J. Verbeeck, *Nat. Commun.* **8**, 14999 (2017).